13. Eloísa Medina, M., Iglesias, M., Gutiérrez-Puebla, E. & Angeles Monge, M. Solvothermal synthesis and structural relations among three anionic aluminophosphates; catalytic behaviour. *J. Mater. Chem.* **14,** 845–850 (2004).
14. Huo, Q. *et al.* Synthesis and characterization of a novel extra large ring of aluminophosphate JDF-20. *Chem. Commun.* 875–876 (1992).
15. Yu, J. *et al.* $Al_{16}P_{20}O_{80}H_4.4C_6H_{18}N_2$: A new microporous aluminophosphate containing intersecting 12- and 8-membered ring channels. *Chem. Mater.* **10,** 1208–1211 (1998).
16. Estermann, M., McCusker, L. B., Baerlocher, C., Merrouche, A. & Kessler, H. A synthetic gallophosphate molecular-sieve with a 20-tetrahedral-atom pore opening. *Nature* **352,** 320–323 (1991).
17. Camblor, M. A., Villaescusa, L. A. & Diaz-Cabanas, M. J. Synthesis of all-silica and high-silica molecular sieves in fluoride media. *Top. Catal.* **9,** 59–76 (1999).
18. Richardson, J. W. Jr, Pluth, J. J. & Smith, J. V. Rietveld profile analysis of calcined $AlPO_4$-11 using pulsed neutron powder diffraction. *Acta Crystallogr. B* **44,** 367–373 (1988).
19. Oliver, S., Kuperman, A., Lough, A. & Ozin, G. A. Synthesis and characterization of a fluorinated anionic aluminophosphate framework UT-6, and its high-temperature dehydrofluorination to $AlPO_4$-CHA. *J. Mater. Chem.* **7,** 807–812 (1997).
20. Feng, P., Bu, X., Gier, T. E. & Stucky, G. D. Amine-directed syntheses and crystal structures of phosphate-based zeolite analogs. *Microporous Mesoporous Mater.* **23,** 221–229 (1998).
21. Taulelle, F. *et al.* Isomerization of the prenucleation building unit during crystallization of $ALPO_4$-CJ2: An MQMAS, CP-MQMAS, and HETCOR NMR study. *J. Am. Chem. Soc.* **121,** 12148–12153 (1999).
22. Robson, H. in *Verified Synthesis of Zeolitic Materials* (ed. Robson, H.) 45–46 (Elsevier, Amsterdam, 2001).
23. Cammarata, L., Kazarian, S. G., Salter, P. A. & Welton, T. Molecular states of water in room temperature ionic liquids. *Phys. Chem. Chem. Phys.* **3,** 5192–5200 (2001).
24. Hanke, C. G. & Lynden-Bell, R. M. A simulation study of water-dialkylimidazolium ionic liquid mixtures. *J. Phys. Chem. B* **107,** 10873–10878 (2003).
25. Lobo, R. F., Zones, S. I. & Davis, M. E. Structure-direction in zeolite synthesis. *J. Inclus. Phenom. Mol.* **21,** 47–78 (1995).
26. Del Popolo, M. G. & Voth, G. A. On the structure and dynamics of ionic liquids. *J. Phys. Chem. B* **108,** 1744–1752 (2004).
27. Kirchner, R. M. & Bennett, J. M. The structure of calcined $AlPO_4$-41: A new framework topology containing one-dimensional 10-ring pores. *Zeolites* **14,** 523–528 (1994).
28. Delgado Friedrichs, O., Dress, A. W. M., Huson, D. H., Klinowski, J. & Mackay, A. L. Systematic enumeration of crystalline networks. *Nature* **400,** 644–657 (1999).
29. Wasserscheid, P. & Welton, T. *Ionic Liquids in Synthesis* Ch. 2.1.2, 9–12 (Wiley-VCH, Weinheim, Germany, 2003).

Supplementary Information accompanies the paper on **www.nature.com/nature**.

Acknowledgements We thank C. Hardacre (Queen's University, Belfast) and D. Cole-Hamilton (University of St Andrews) for discussions. We thank the CCLRC and S. Teat for access to the Synchrotron Radiation Source (Daresbury) and the EPSRC and D. Apperley for access to solid-state NMR. R.E.M. was supported by a Royal Society University Research Fellowship.

Competing interests statement The authors declare that they have no competing financial interests.

Correspondence and requests for materials should be addressed to R.E.M. (rem1@st-and.ac.uk).

Similar meltwater contributions to glacial sea level changes from Antarctic and northern ice sheets

Eelco J. Rohling[1], Robert Marsh[1], Neil C. Wells[1], Mark Siddall[1,2] & Neil R. Edwards[2,3]

[1]*Southampton Oceanography Centre, Southampton SO14 3ZH, UK*
[2]*Climate and Environmental Physics, University of Bern, Sidlerstrasse 5, and*
[3]*NCCR-Climate, University of Bern, Erlachstrasse 9a, CH-3012 Bern, Switzerland*

The period between 75,000 and 20,000 years ago was characterized by high variability in climate[1–12] and sea level[13,14]. Southern Ocean records of ice-rafted debris[15] suggest a significant contribution to the sea level changes from melt water of Antarctic origin, in addition to likely contributions from northern ice sheets, but the relative volumes of melt water from northern and southern sources have yet to be established. Here we simulate the first-order impact of a range of relative meltwater releases from the two polar regions on the distribution of marine oxygen isotopes, using an intermediate complexity model. By comparing our simulations with oxygen isotope data from sediment cores, we infer that the contributions from Antarctica and the northern ice sheets to the documented sea level rises between 65,000 and 35,000 years ago[13] were approximately equal, each accounting for a rise of about 15 m. The reductions in Antarctic ice volume implied by our analysis are comparable to that inferred previously for the Antarctic contribution to meltwater pulse 1A (refs 16, 17), which occurred about 14,200 years ago, during the last deglaciation.

Greenland ice-core records show strong climate fluctuations between 75 and 20 kyr BP: the Dansgaard–Oeschger (DO) cycles[1–3]. Abrupt warmings of 6–10 °C occurred throughout the mid- to high-latitude North Atlantic region at a spacing of about 1,500 yr (refs 4, 5). Each initiated a relatively warm DO interstadial, during which a gradual cooling trend developed that eventually culminated in rapid 'collapse' to the next cold DO stadial. DO-style variability was widespread throughout the northern hemisphere and beyond[5–9].

Antarctic ice-core records follow a different 'rhythm', with fewer and temporally more symmetrical climate fluctuations. The timing relationship between DO-style and Antarctic-style fluctuations was established with the use of atmospheric methane data from ice cores[10] and was corroborated by work on marine sediment core MD952042 from 3,146 m depth off Portugal[12]. The $\delta^{18}O$ record for surface-water planktonic foraminifera in MD952042 shows DO-style variability, whereas that for bottom-dwelling benthic foraminifera mimics Antarctic-style variability[12]. The latter is observed also in SW Pacific core MD972120 from 1,210 m depth[9], showing the global nature of the benthic signal.

The widespread benthic $\delta^{18}O$ signal suggests a relationship between variations in southern high-latitude climate and global ice volume (sea level). However, benthic $\delta^{18}O$-based sea level reconstructions might be biased by deep-sea temperature changes: 1 °C error translates to about 30 m uncertainty in sea level. Efforts to separate ice volume from temperature influences on benthic $\delta^{18}O$ indicate rapid and high-amplitude ice-volume variability during the last glacial cycle[14]. Independent sea level quantification from the Red Sea method is coherent with both the absolute values from fossil reef data and the structure of benthic $\delta^{18}O$ records[13]. It indicates that sea level rose by about 30 m, at 2 m per century, in association with the 2–3 °C warming of Antarctic climate events A1–4 (Fig. 1a)[13].

Although the Antarctic-style timing of sea level change might imply Antarctic ice-volume variations, it is equally possible that southern high-latitude climate fluctuations were driven by oscillations in climate and ice volume on the Northern Hemisphere[18,19], because Antarctic ice volume is often considered relatively stable, with its full glacial–interglacial variability contributing less than 25 m to the roughly 120 m global sea level change[20–24], and because models forced with meltwater additions into the North Atlantic and Arctic show interhemispheric temperature fluctuations similar to those observed in ice cores[18,19]. However, recent work has challenged the notion of Antarctic stability on the basis of distinct ice-rafted debris (IRD) peaks in Southern Ocean records, preceded by −0.5‰ to −0.9‰ shifts in surface-water foraminiferal $\delta^{18}O$ (ref. 15; Fig. 1c). A predominantly Antarctic origin has also been inferred for meltwater pulse (mwp) 1A, a sea level rise of about 20 m in about 500 yr during the last deglaciation[16,17].

Here we assess the origins of the meltwater pulses that caused sea level rises associated with Antarctic warming events A1–4 (Fig. 1a), by using marine $\delta^{18}O$ as a sensitive tracer for input of isotopically light high-latitude melt water. Away from its surface-bound source and sink terms, $\delta^{18}O$ in sea water behaves as a conservative, passive tracer. Crucially, past seawater $\delta^{18}O$ changes are reflected in $\delta^{18}O$

records from fossil foraminiferal shells (carbonate) in sediment cores, the only significant complication being a temperature-dependent $\delta^{18}O_{water}$ to $\delta^{18}O_{carbonate}$ fractionation (1‰ shift to lighter $\delta^{18}O_c$ values for every 4 °C warming). Bearing this in mind, we use fossil records to validate $\delta^{18}O$ distribution simulations that we develop using an Earth System Model of Intermediate Complexity (EMIC), namely the three-dimensional ocean/atmosphere/sea-ice model C-GOLDSTEIN[25,26] (Methods). To assess the impacts of meltwater influxes at typical magnitudes and rates (Fig. 1), we impose a total release of 345 Sv ($1\ Sv = 10^6\ m^3\ s^{-1}$) years (30 m sea level rise over 1,500 yr). Robustness of results is assessed through sensitivity analyses (Methods), and maps and profiles are given for a variety of scenarios in Supplementary Information. We initially focus on $\delta^{18}O_w$ (Figs 2 and 3a, b) but also consider $\delta^{18}O_c$ maps and profiles that rely on modelled temperatures, based on $\Delta\delta^{18}O_c = \Delta\delta^{18}O_w - (1/4)\Delta T$ (Fig. 3b–d).

Model simulations are validated with foraminiferal $\delta^{18}O_c$ records from the wider Atlantic Ocean (equivalent to the Arctic plus the North and South Atlantic) through the intervals of the A1–4 warming events, with emphasis on the upper 2,000 m, where the most distinctive signal amplitudes are found. Key $\delta^{18}O_c$ observations for deep-water (benthic foraminifera) and surface-

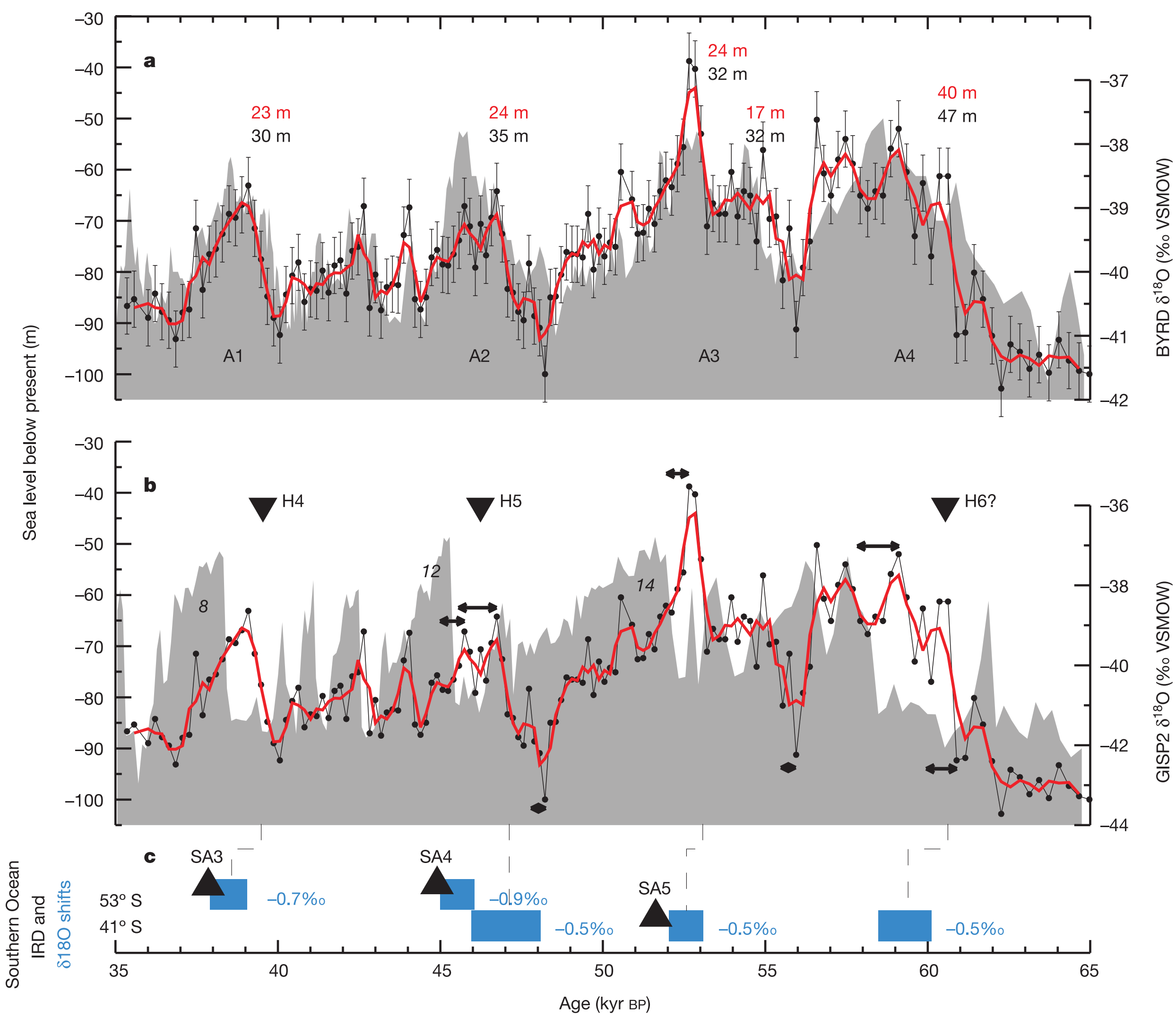

Figure 1 Comparison of the Red Sea sea level record with Antarctic and Greenland ice-core records and with the timing of both North Atlantic (Heinrich; H) and Southern Ocean (SA) IRD events. **a**, Sea level reconstruction from the Red Sea method (black dots and line)[13] compared with Antarctic ice-core $\delta^{18}O$ temperature proxy data (grey) from the BYRD-station ice core (80.0° S, 119.5° W). Error bars indicate 1 standard deviation. **b**, As **a**, but for Greenland Ice Sheet Project 2 (GISP2, 72.6° N, 38.5° W) ice-core $\delta^{18}O$ (grey). Ice-core data as synchronized to the GISP2 timescale using variations in atmospheric methane concentrations[10]. Red lines represent three-point (about 500-yr) moving averages of the sea level record, which smoothes inter-sample variability within bounds of the 1σ interval (±5.5 m) that applies to the sea level reconstruction[13]. Red numbers in **a** indicate magnitudes of increases in sea level according to the smoothed record, whereas black numbers relate to the unsmoothed data. Inverted triangles in **b** indicate the occurrence of North Atlantic Heinrich Events H4, H5 and tentatively H6, relative to the GISP2 record[8]. Italic numbers identify main Dansgaard–Oeschger interstadials 8, 12 and 14. Double-headed arrows illustrate dating differences[13] between the original correlation of the Red Sea sea level record to BYRD (as in **a**) and after tuning to a benthic $\delta^{18}O$ record[12]. **c**, Schematic representation of intervals of IRD, marked by triangles and SA numbers, as well as intervals with negative $\delta^{18}O$ shifts in planktonic foraminiferal calcite at 41° and 53° S in the South Atlantic sector[15]. These events were placed within our time frame by graphically transferring the positions of the events relative to the GISP2 $\delta^{18}O$ record as originally reported[15]. Dashed lines indicate possible correlations to the sea level record. A maximum disagreement is suggested of roughly 1,000 yr, which seems reasonable given the inherent uncertainties in both the sea level chronology (**b**, and ref. 13) and Southern Ocean records[15]. VSMOW, Vienna Standard Mean Ocean Water.

water (planktonic foraminifera) are reviewed in Supplementary Information, and appropriate ranges for the observations are represented with coloured circles in Fig. 3b–d.

For 100% northern meltwater release, the model shows a collapse of the Atlantic meridional overturning circulation (MOC) (Fig. 2d). This 'traps' the meltwater influence in the top 1,200 m of the Atlantic, and particularly the top 400 m, so that the Atlantic-wide mean $\delta^{18}O_w$ anomaly in the upper 400 m reaches -1.9‰, whereas the mean value between 400 and 1,200 m is -0.9‰ (Fig. 2a). The most extreme $\delta^{18}O_c$ values produced by this scenario in the surface North Atlantic are of the order of -5‰. This simulated range of values is incompatible with the observations (Fig. 3c).

For 100% meltwater release around Antarctica, the Atlantic MOC intensifies to about 19 Sv within about 100 yr, followed by gradual weakening over the next couple of centuries (Fig. 2d). There is no pooling of melt water at the surface in the North Atlantic, and $\delta^{18}O_w$ anomalies do not exceed -0.5‰ (Fig. 2b and Supplementary Information). This scenario fails to capture the considerable regional $\delta^{18}O_c$ anomalies that have been observed in the North Atlantic[11] (Supplementary Information), and also produces deep-water $\delta^{18}O_c$ fields that are very different from the observations (Fig. 3d).

Meltwater discharge into the NW Atlantic during Heinrich events of IRD deposition (Fig. 1) may have caused a global sea level rise of up to 15 m within 500 ± 250 yr (ref. 11). Our next experiment therefore considered 50% release into the North Atlantic and 50% around Antarctica. In the absence of clearly documented phase relationships between northern and southern meltwater releases, we specify both as synchronous and lasting 1,500 yr. Different phasing and durations were considered separately (below).

The 50:50 scenario shows a collapse of the Atlantic MOC (Fig. 2d), causing an Atlantic-wide mean $\delta^{18}O_w$ anomaly of -1.2‰ in the upper 400 m, and -0.8‰ between 400 and 1,200 m (Figs 2c and 3a, b). The most extreme North Atlantic $\delta^{18}O_c$ values approach -3‰. Cooling in much of the North Atlantic surface to intermediate waters (Fig. 4c, d) would reduce the amplitude of the simulated $\delta^{18}O$ anomalies when recorded in carbonates. Maps and profiles of $\delta^{18}O_c$ show expected anomalies in broad agreement with the observations from sediment cores, although it seems that the model somewhat underestimates cooling to the north of about 60° N (Fig. 3b).

Further experiments at 10% increment changes between the northern and southern inputs corroborate the notion that agreement with the isotope data constrains the meltwater contribution from both regions to roughly equal (50 ± 10%) proportions. This first-order conclusion of roughly equal contributions is not significantly affected by changes in the $\delta^{18}O$ values of the northern and southern meltwater components to -30‰ and -50‰, respectively (Supplementary Information).

How well does the 50:50 scenario simulate the bipolar temperature seesaw inferred from Greenland and Antarctic ice cores[10]? It shows robust cooling in the north and warming in the south (Fig 4a, b), but the simulated southern warming underestimates the 2–3 °C deduced from ice cores[27]. Note, however, that all experiments concern highly schematic scenarios in a model of intermediate complexity. Inclusion of the radiative effects of a simple 20 p.p.m.v. CO_2 fluctuation[28], for example, brings the modelled temperature amplitudes closer to observed values (Fig. 4e, f), indicating that future models should include a reasonable carbon cycle. Separate tests with offset phasing and different durations of the northern and southern meltwater releases highlight a dominant control on the temporal structure of the temperature signals, making these parameters prime targets for future data collection.

In dynamical terms, our experiments simulate a 'realistic' range of isotope values when we apply sufficient meltwater release into the North Atlantic to severely reduce or just collapse the Atlantic MOC. To approximate the bipolar temperature seesaw also, a collapse seems to be required. The model shows a robust collapse when about one-third of the stipulated meltwater release is specified through any route into the North Atlantic (either at high latitudes or through the Gulf of Mexico) (Fig. 2d, and Methods), similar

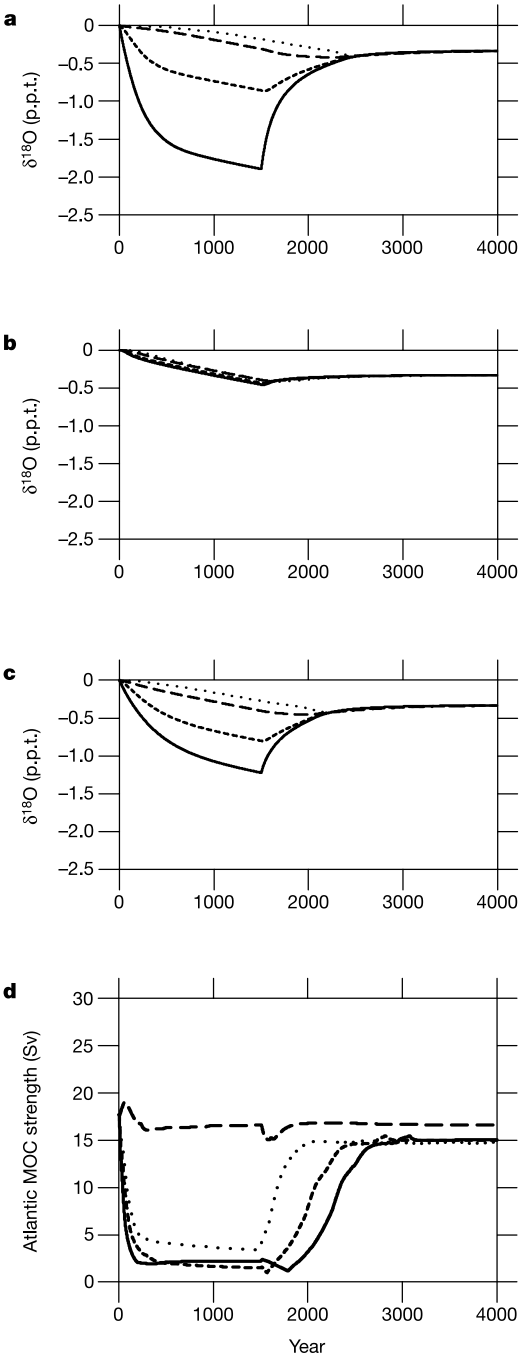

Figure 2 Development of Atlantic-wide mean $\delta^{18}O$ values with time in the upper (solid lines), intermediate (broken lines), deep (dashed lines) and bottom (dotted lines) waters. All simulations performed with the EMIC concern a total meltwater release of 0.23 Sv over 1,500 yr. **a**–**c**, Three scenarios: 100% release into the North Atlantic (**a**), 100% release around Antarctica (**b**), and 50% release into the North Atlantic and 50% around Antarctica (**c**). **d**, Changes in the MOC intensity for the various scenarios, including a 30:70 experiment that closely approximates the collapse of the Atlantic MOC. More detailed graphs of results are given in Supplementary Information. Solid line, 100% release into the Atlantic; broken line, 50% release into the North Atlantic and 50% around Antarctica; dotted line, 30% release into the North Atlantic and 70% around Antarctica; dashed line, 100% release around Antarctica.

to the freshwater fluxes required for a collapse in previous studies[19,29].

For the first time we find a meltwater scenario that reasonably approximates the main characteristics of the sea level, marine $\delta^{18}O$, and seesaw data. Our robust first-order conclusion is that the investigated increases in sea level (Fig. 1) resulted from both northern and southern meltwater contributions, in roughly equal proportions. The magnitude and rate of the implied Antarctic meltwater pulses are comparable to those suggested for mwp 1A (refs 16, 17). We find that such events occurred at a 5–8-kyr spacing between 60 and 35 kyr BP. Three events peaked about 1,000 yr before major DO interstadials (Fig. 1b). This is sufficiently similar to the

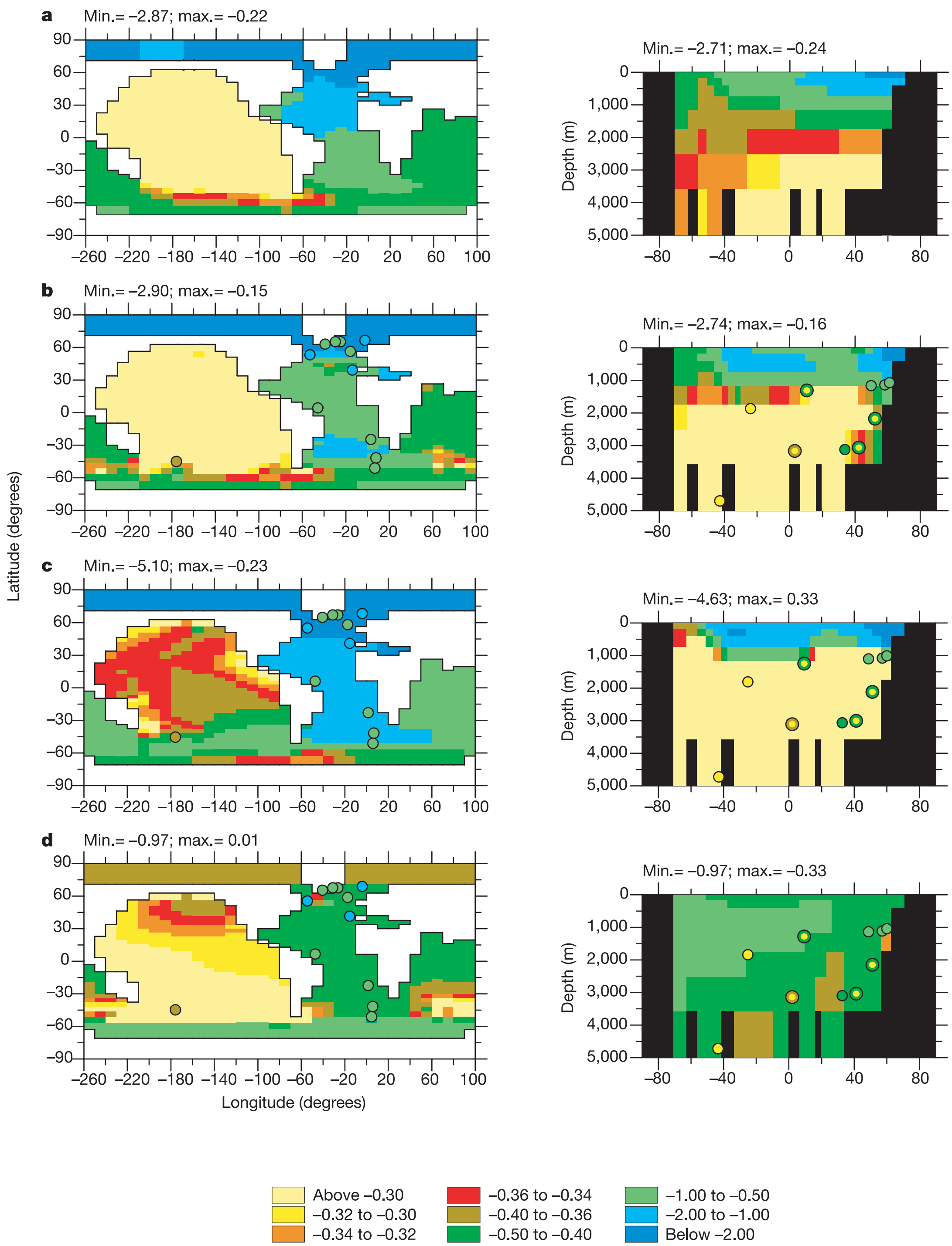

Figure 3 Horizontal (at 80 m depth) and vertical (along 25° W) distributions of $\delta^{18}O$ after 1,500 yr of 0.23 Sv meltwater release. **a**, **b**, $\delta^{18}O_w$ and $\delta^{18}O_c$ for the experiment with 50% meltwater release into the North Atlantic and 50% around Antarctica: **a**, $\delta^{18}O_w$, and **b**, $\delta^{18}O_c$. **c**, **d**, Simulated $\delta^{18}O_c$ for experiments with 100% meltwater release into the North Atlantic (**c**) and 100% around Antarctica (**d**). Circles give values (or wider ranges in the case of composite circles) observed in sediment records, as discussed in Supplementary Information. In the vertical profiles, observations have been laterally projected onto the 25° W transect. In the right-hand panels, the *x* axes indicate latitude, with negative values for the Southern Hemisphere.

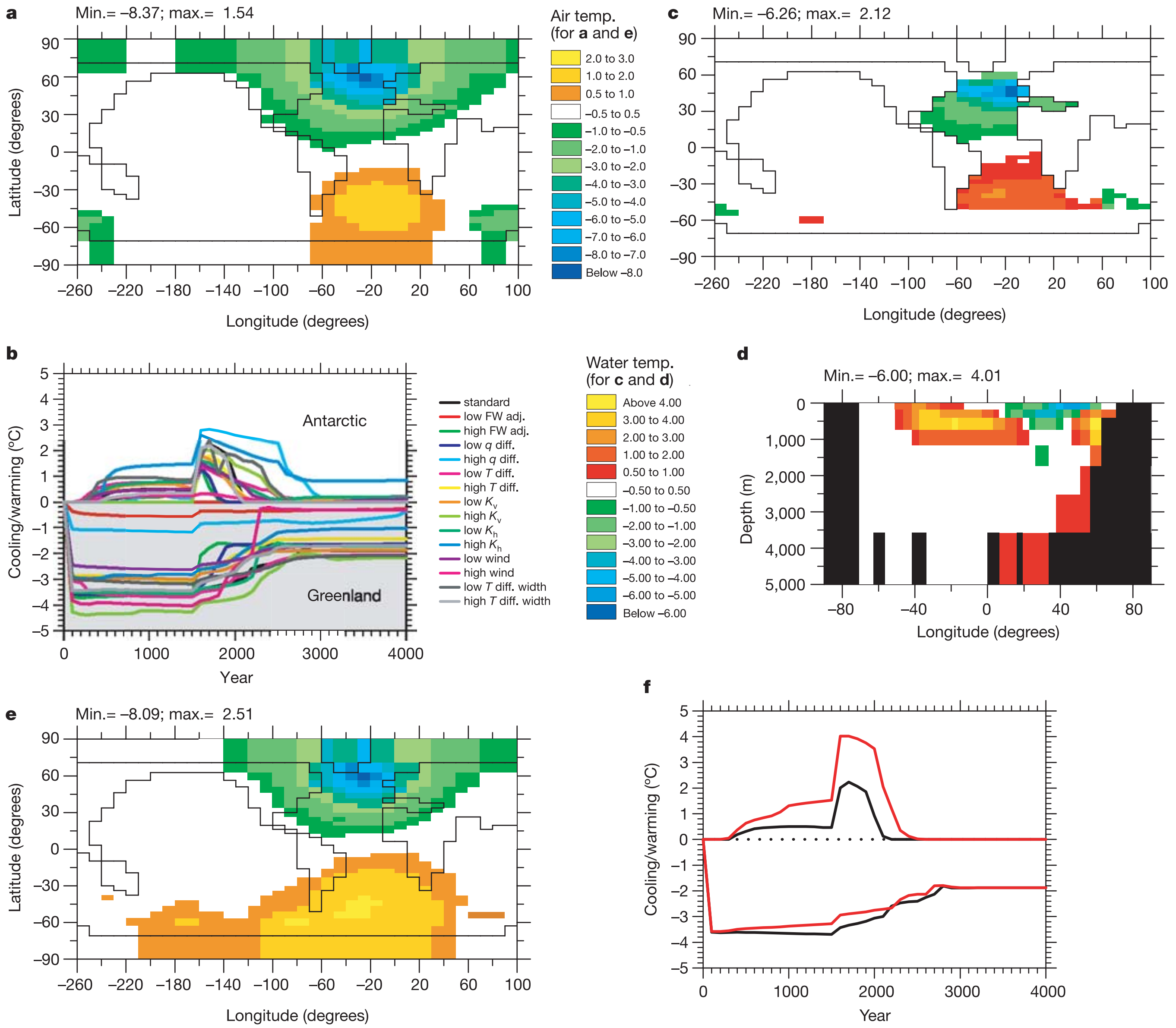

Figure 4 Temperature simulations (at year 1,000) in the 50:50 model, for 0.23 Sv meltwater release. **a**, Air temperature anomaly. **b**, Air temperature development (averages between 20° and 60° W at 70–90° N and 70–90° S) plotted against time in a suite of simulations for the 50:50 model using a wide variety of model parameter settings, illustrating robustness of the result (Methods). FW concerns Atlantic–Pacific exchange of moisture, *q* is atmospheric moisture diffusivity, *T* controls diffusive atmospheric heat transport, and K_v and K_h are diffusivity coefficients for diapycnal and isopycnal mixing, respectively. **c**, Ocean temperature anomaly at 80 m depth. **d**, Ocean temperature anomaly in a section along 25° W longitude. **e**, As **a** but for a scenario with atmospheric [CO_2] increasing linearly by 20 p.p.m.v. over 1,500 yr, and then decreasing linearly to its initial value by year 3000, in a schematic representation of the [CO_2] changes associated with Antarctic temperature changes[28]. **f**, Plot comparing air temperature changes as in **b**, contrasting the results including (red) and excluding (black) the [CO_2] changes described for **e**.

roughly 500-yr lag between mwp 1A (refs 16, 17) and the Bølling–Allerød interstadial to suggest a comparable causal relationship through changes in the global thermohaline circulation[17].

The inferred roughly 15 m sea level magnitude of the investigated Antarctic ice-volume reductions is towards the high end of current estimates for the glacial 'excess' ice volume on Antarctica[20–24]. It implies that virtually the entire glacial excess might have been involved in millennial-scale variability. □

Methods

The EMIC used here is the three-dimensional ocean/atmosphere/sea ice model C-GOLDSTEIN version 1 (refs 25, 26). The ocean component is a frictional geostrophic model with eddy-induced and isopycnal mixing—appropriate physics to model the global-scale thermohaline circulation properly. Simplified physics and low resolution (36 × 36 equal-area cells with eight vertical levels) make the model highly efficient. The ocean is coupled to a two-dimensional energy and moisture balance atmosphere and a dynamic and thermodynamic sea-ice component[26].

The model is spun up under simple glacial boundary conditions: atmospheric CO_2 concentration is held constant at 210 p.p.m., and planetary albedo over land poleward of 50° N is increased by 0.18 to mimic ice sheets. To account for the generally low glacial sea level position, the Bering Strait is kept closed in the glacial runs, including all meltwater experiments. The values for 12 key model parameters are the posterior ensemble-mean estimates obtained in a recent tuning exercise, using an ensemble Kalman filter[25]. In a 'standard' spin-up, the model is integrated for 4,000 yr, sufficiently long to equilibrate the global thermohaline circulation (THC). Under glacial boundary conditions, the model simulates air temperatures up to 15 °C lower (at high latitudes), and Atlantic sinking of similar strength but shifted 5–10° south compared with a present-day climate simulation.

To investigate post-collapse recovery of the Atlantic overturning (see below), we performed 14 additional spin-up experiments in which 7 of the 12 key parameters (those exerting most control on the THC) were increased or decreased in turn by 2 standard deviations of the ensemble-mean estimates. The Atlantic overturning across these spin-up experiments varies in the range 3–23 Sv (although 12 of the 14 experiments lie in the relatively narrow range 12–20 Sv; see illustrations in Supplementary Information).

From the end of each spin-up, we performed a series of 4,000-yr meltwater release experiments, in each case adding 0.23 Sv to the local surface freshwater flux over 1,500 yr and 'tagging' the melt water with a $\delta^{18}O$ value of −40‰ (the background $\delta^{18}O$ value is assumed zero everywhere). The model offers insight into the likely spatial and depth-dependent distributions of meltwater-induced $\delta^{18}O$ anomalies, while accounting for the impacts of ocean dynamics on the result. Sensitivity tests have been undertaken with $\delta^{18}O$ values of −30‰ and −50‰. The main experiments considered a series of different meltwater release scenarios: 100% in the North Atlantic zone 50–70° N (additional experiments considered partial or complete release into the Gulf of Mexico); a 50:50 split between the North Atlantic and around Antarctica; 100% around Antarctica; and 20:80, 30:70 and 40:60 splits between the North Atlantic and Antarctica. For diagnostic purposes we averaged $\delta^{18}O$ over four major basins (Atlantic, Southern Ocean, Pacific, Indian) in four layers (upper, 0–411 m; intermediate, 411–1,158 m; deep, 1,158–2,520 m; bottom, 2,520–5,000 m).

The model has a simplified atmosphere, no carbon cycle (that is, no CO_2 and CH_4 feedbacks), no interactive ice sheets and no insolation changes or solar variability. The scenarios presented are part of a suite of experiments in which the proportions between North Atlantic and Antarctic meltwater combinations were varied in 10% increments. The scenarios comprise constant and simultaneous meltwater fluxes into the North Atlantic and (equally distributed) around Antarctica. As part of the sensitivity analyses, some scenarios have also been run with differently phased northern and southern inputs. In total, nearly 150 4,000-yr simulations have been performed to ensure that the results discussed in this paper are robust with regard to all feasible combinations for the key model parameters.

In the EMIC, the Atlantic overturning is very sensitive to the location of imposed meltwater releases, similarly to previous studies[17,29,30]. In our extreme case with 100% meltwater release into the North Atlantic, the Atlantic overturning circulation collapses rapidly (Fig. 2), preserving a strong local $\delta^{18}O$ signal in surface layers during, and shortly after, the period of freshwater release (Fig. 3a). The same collapse (and corresponding isotopic signal) is obtained with every combination of key model parameters considered here (Supplementary Fig. 4). Similar tests for robustness have been made for the 50:50, 40:60 and 30:70 scenarios. These experiments confirm the robustness of our main results, namely the collapse of Atlantic overturning under a sustained local freshwater flux anomaly of about 0.1 Sv, in agreement with other studies[29,30].

Received 3 March; accepted 16 July 2004; doi:10.1038/nature02859.

1. Langway, C. C. Jr, Oeschger, H. & Dansgaard, W. (eds) *Greenland Ice Core: Geophysics, Geochemistry, and the Environment* (Geophys. Monogr. 33, Am. Geophys. Union, Washington DC, 1985).
2. Grootes, P. M., Stuiver, M., White, J. W. C., Johnsen, S. & Jouzel, J. Comparison of oxygen isotope records from the GISP2 and GRIP Greenland ice cores. *Nature* **366,** 552–554 (1993).
3. Dansgaard, W. *et al.* Evidence for general instability of past climate from a 250 kyr ice core. *Nature* **364,** 218–219 (1993).
4. Rahmstorf, S. Timing of abrupt climate change: a precise clock. *Geophys. Res. Lett.* **30** doi:10.1029/2003GL017115 (2003).
5. Broecker, W. S. Abrupt climate change: causal constraints provided by the paleoclimate record. *Earth Sci. Rev.* **51,** 137–154 (2000).
6. Voelker, A. H. *et al.* Global distribution of centennial-scale records for marine isotope stage (MIS) 3: a database. *Quat. Sci. Rev.* **21,** 1185–1212 (2002).
7. Leuschner, D. C. & Sirocko, F. The low-latitude monsoon climate during Dansgaard–Oeschger cycles and Heinrich events. *Quat. Sci. Rev.* **19,** 243–254 (2000).
8. Rohling, E. J., Mayewski, P. A. & Challenor, P. On the timing and mechanism of millennial-scale climate variability during the last glacial cycle. *Clim. Dyn.* **20,** 257–267 (2003).
9. Pahnke, K., Zahn, R., Elderfield, H. & Schultz, M. 340,000-year centennial-scale marine record of Southern Hemisphere climatic oscillation. *Science* **301,** 948–952 (2003).
10. Blunier, T. *et al.* Asynchrony of Antarctic and Greenland climate change during the last glacial period. *Nature* **394,** 739–743 (1998).
11. Hemming, S. R. Heinrich events: Massive detritus layers of the North Atlantic and their global climate impact. *Rev. Geophys.* **42,** RG1005, doi: 10.1029/2003RG 000128 (2004).
12. Shackleton, N. J., Hall, M. A. & Vincent, E. Phase relationships between millennial-scale events 64,000–24,000 years ago. *Paleoceanography* **15,** 565–569 (2000).
13. Siddall, M. *et al.* Sea-level fluctuations during the last glacial cycle. *Nature* **423,** 853–858 (2003).
14. Cutler, K. B. *et al.* Rapid sea-level fall and deep-ocean temperature change since the last interglacial period. *Earth Planet. Sci. Lett.* **206,** 253–271 (2003).
15. Kanfoush, S. L. *et al.* Millennial-scale instability of the Antarctic ice sheet during the last glaciation. *Science* **288,** 1815–1818 (2000).
16. Clark, P. U., Mitrovica, J. X., Milne, G. A. & Tamisiea Sea-level fingerprinting as a direct test for the source of global meltwater pulse 1A. *Science* **295,** 2438–2441 (2002).
17. Weaver, A. J., Saenko, O. A., Clark, P. U. & Mitrovica, J. X. Meltwater pulse 1A from Antarctica as a trigger of the Bølling-Allerød warm interval. *Science* **299,** 1709–1713 (2003).
18. Stocker, T. F. & Johnsen, S. J. A minimum thermodynamic model for the bipolar seesaw. *Paleoceanography* **18,** PA1087, doi:10.1029/2003PA000920 (2003).
19. Ganopolski, A. & Rahmstorf, S. Rapid changes of glacial climate simulated in a coupled climate model. *Nature* **409,** 153–158 (2001).
20. Barrett, P. J. Antarctic palaeoenvironment through Cenozoic times—a review. *Terra Antartica* **3,** 103–119 (1996).
21. Peltier, W. R. Ice Age palaeotopography. *Science* **265,** 195–201 (1994).
22. Huybrechts, P. Sea-level changes at the LGM from ice-dynamic reconstructions of the Greenland and Antarctic ice sheets during the glacial cycles. *Quat. Sci. Rev.* **21,** 203–231 (2002).
23. Denton, G. H. & Hughes, T. J. Reconstructing the Antarctic Ice Sheet at the Last Glacial Maximum. *Quat. Sci. Rev.* **21,** 193–202 (2002).
24. Anderson, J. B., Shipp, S. S., Lowe, A. L., Wellner, J. S. & Mosola, A. B. The Antarctic Ice Sheet during the Last Glacial Maximum and its subsequent retreat history: a review. *Quat. Sci. Rev.* **21,** 49–70 (2002).
25. Annan, J. D., Hargreaves, J. C., Edwards, N. R. & Marsh, R. Parameter estimation in an intermediate complexity earth system model using an ensemble Kalman filter. *Ocean Model.* (in the press).
26. Edwards, N. R. & Marsh, R. Uncertainties due to transport parameter sensitivity in an efficient 3-D ocean-climate model. *Clim. Dyn.* (submitted) (2004).
27. Stenni, B. *et al.* A late-glacial high-resolution site and source temperature record derived from the EPICA Dome C isotope records (East Antarctica). *Earth Planet. Sci. Lett.* **217,** 183–195 (2003).
28. Indermühle, A., Monnin, E., Stauffer, B., Stocker, T. F. & Wahlen, M. Atmospheric CO_2 concentration from 60 to 20 kyr BP from the Taylor Dome ice core, Antarctica. *Geophys. Res. Lett.* **27,** 735–738 (1999).
29. Rahmstorf, S. Bifurcations of the Atlantic thermohaline circulation in response to changes in the hydrological cycles. *Nature* **378,** 145–149 (1995).
30. Rahmstorf, S. Rapid climate transitions in a coupled ocean–atmosphere model. *Nature* **372,** 82–85 (1994).

Supplementary Information accompanies the paper on **www.nature.com/nature**.

Acknowledgements We thank T. Stocker, J. Thomson, A.P. Roberts, W. Broecker and N. Shackleton for suggestions. All authors contributed equally to this work.

Competing interests statement The authors declare that they have no competing financial interests.

Correspondence and requests for materials should be addressed to E.J.R. (e.rohling@soc.soton.ac.uk).

A Middle Jurassic 'sphenosuchian' from China and the origin of the crocodylian skull

James M. Clark[1], **Xing Xu**[2*], **Catherine A. Forster**[3] **& Yuan Wang**[2]

[1]*Department of Biological Sciences, George Washington University, Washington DC 20052, USA*
[2]*Institute of Vertebrate Paleontology and Paleoanthropology, Chinese Academy of Sciences, 142 Xiwai Street, Beijing, 100044, China*
[3]*Department of Anatomical Sciences, Stony Brook University, Stony Brook, New York 11794, USA*

* Present address: Department of Paleontology, American Museum of Natural History, 79th Street at Central Park West, New York 10024, USA

The skull of living crocodylians is highly solidified and the jaw closing muscles are enlarged[1], allowing for prey capture by prolonged crushing between the jaws. Living species are all semi-aquatic, with sprawling limbs and a broad body that moves mainly from side-to-side[2]; however, fossils indicate that they evolved from terrestrial forms. The most cursorial of these fossils[3–6] are small, gracile forms often grouped together as the Sphenosuchia, with fully erect, slender limbs; their relationships, however, are poorly understood[5,7–10]. A new crocodylomorph from deposits in northwestern China of the poorly known Middle Jurassic epoch possesses a skull with several adaptations typical of living crocodylians. Postcranially it is similar to sphenosuchians but with even greater adaptations for cursoriality in the forelimb. Here we show, through phylogenetic analysis, that it is the closest relative of the large group Crocodyliformes, including living crocodylians. Thus, important features of the modern crocodylian skull evolved during a phase when the postcranial skeleton was evolving towards greater cursoriality, rather than towards their current semi-aquatic habitus.

The Sphenosuchia includes nine monotypic genera comprising the most basal members of the Crocodylomorpha, but its monophyly has been controversial. Sphenosuchians were once[7] thought to be a paraphyletic assemblage with some taxa closer to the large group Crocodyliformes. Later evidence suggested that Sphenosuchia is a monophyletic group[5,8–10], but some analyses found no resolution owing to conflicting data[6]. Members of the Crocodyliformes are diagnosed by a large suite of features[11], some of which are related to the solidifying of intracranial joints and an increase in the

Supplementary Information to:

Similar melt-water contributions from Antarctic and Northern ice sheets to glacial sea-level variability

Eelco J. Rohling, Robert Marsh, Neil C. Wells, Mark Siddall, and Neil R. Edwards

Part 1 – Review of Atlantic benthic and planktonic foraminiferal $\delta^{18}O$ data used to validate the model results presented in this study.
Part 2 – Relevant information, maps, and profiles concerning the Earth System Model of Intermediate Complexity (EMIC) and the various experiments performed.

Part 1

When validating the $\delta^{18}O$ anomalies simulated for the various scenarios with highly-resolved Atlantic $\delta^{18}O$ records, we focus on events A1 (~39 ka BP) and A2 (~47 ka BP), since age control is better for younger events. The observations are discussed below in general terms, and those used in main-text Figure 3 are presented in Table 1.

Concerning benthic foraminiferal records, Core 1225 from the Denmark Strait, with data for the surface and 1683m water depth, shows $\delta^{18}O$ shifts of –0.5 to –0.7‰ around the target intervals (mostly around the time of Heinrich events)[31]. Core NA87-22 from the NE Atlantic has maximum $\delta^{18}O$ shifts at 2160m water depth of order –0.5‰[Ref.32]. North of Newfoundland, $\delta^{18}O$ shifts of about –1‰ were found at 1251m water depth[33]. Core MD35003-4 from east of the island of Grenada provides a $\delta^{18}O$ record for 1299m water depth that lacks a significant shift for event A2, but shifts by –0.5‰ at A1[Ref.34]. Finally, benthic $\delta^{18}O$ records for four cores that cover a depth range of 1967-3169m from N to S through the entire Atlantic Ocean provide evidence for two consistent light $\delta^{18}O$ peaks: LP1 and LP2[Ref.35]. Using recently proposed GISP2-equivalent ages for Heinrich Events (iceberg surges) in the N Atlantic[8] to translate the ages to the GISP2-equivalent age model used here, we derive ages of about 39-36 and 48-45 ka BP for LP1 and LP2, in agreement with Little et al.[36]. Both $\delta^{18}O$ shifts reach –0.3 to –0.5‰[Ref.35].

In planktonic foraminiferal records, shifts to light $\delta^{18}O$ values have been found in association with Heinrich events, reaching maximum amplitudes around –1.0‰ in Denmark Strait and the Irminger Sea[31,37,38], the Nordic Seas[32,39], and the S. Labrador Sea[33]. In the latter, the anomalies can exceed –1.5‰[Ref.33]. Such magnitudes may also be reached in the main N Atlantic IRD belt, particularly between 45 and 50ºN[11]. In core MD95-2042, off S Portugal, the planktonic $\delta^{18}O$ record shows an extremely strong DO-style pattern, with light anomalies at times of Heinrich events that are typically smaller than –1.0‰ [Ref.12], which is also the case in the central N Atlantic at 43ºN[Ref.40]. Near the equator, surface-water $\delta^{18}O$ anomalies at times of Heinrich events do not exceed –0.5‰ [Ref.35].

Table 1. Summary of observations as used in main-text Figure 3.

Core	latitude	longitude	depth (m)	planktonic /benthic	d18O anomaly	Ref.
1225	64°54.3'N	29°17.4'W	1683	P	-0.6 to -1.0	31
1225	64°54.3'N	29°17.4'W	1683	B	-0.5 to -0.7	31
NA87-22	55°29.8'N	14°41.7'W	2161	P	up to -1.0	32
NA87-22	55°29.8'N	14°41.7'W	2161	B	-0.3 to -0.5	32
EW9302-2	48°47.7'N	45°05.09'W	1251	P	-0.8 to -1.6	33
EW9302-2	48°47.7'N	45°05.09'W	1251	B	up to -1.3	33
MD35003-4	12°5.4'N	61°14.6'W	1299	B	up to -0.5	34
SU90-08	43°N	30°W	3080	B	-0.3 to -0.5	35
GEOB1515	4°14.3'N	43°4'W	3169	B	-0.3 to -0.4	35
GEOB1515	4°14.3'N	43°4'W	3169	P	about -0.5	35
GEOB1711	23°18.9'S	12°22.6'E	1967	B	up to -0.3	36
GEOB1711	23°18.9'S	12°22.6'E	1967	P	-0.6 to -0.8	35
MD952042	37°48'N	10°10'W	3146	B	about -0.5	12
MD952042	37°48'N	10°10'W	3146	P	about -1.2	12
MD952010	66°41.05'N	04°33.97'E	1226	P&B	close to -1.0	39
ENAM9321	62°44.3'N	03°59.92'W	1020	P&B	close to -1.0	39
PS2644	67°52.02'N	21°45.92'W	777	P	-0.5 to -1.0*	37
SU90-24	62°40'N	37°22'W	2100	P	-0.7 to -0.8	38
TTN05713/1094	53°2'S	05°1'E	2850	P	-0.5 to -0.9	15
RC11-83	41°36'S	09°48'E	4718	B	about -0.3	41
RC11-83	41°36'S	09°48'E	4718	P	up to -0.6	41
MD972120	45°32.06'S	174°55.85'E	1210	P	about -0.4	9

NB: where there is no clarity about the exact temporal relationship of the isotope anomalies in the cores and the Antarctic (A) climate events, typical magnitudes of the anomalies over the relevant part of the last glacial cycle is used. This mostly affects planktonic anomalies recorded here.

* = rather unclear in the records, and should be treated with caution.

Part 2

The ocean component of C-GOLDSTEIN is a frictional geostrophic model with eddy-induced and isopycnal mixing - appropriate physics to properly model the global-scale thermohaline circulation[42]. The system is closed by a 2-D, energy and moisture balance atmosphere[43] and a dynamic and thermodynamic sea-ice component[44,45]. To supplement the weak moisture transport in the simple atmosphere, a prescribed Atlantic to Pacific flux is added[26]. Parameter values, the dominant source of uncertainty for long-term climate simulations, and the associated uncertainties, have been objectively determined using the Ensemble Kalman Filter[25,46] aided by the extreme efficiency of the model. Melt-water pulse experiments are carried out from a series of glacial initial states (*Methods*). A key factor in these experiments is the Atlantic overturning circulation.

Figures S-1 and S-2 show key aspects of the Atlantic meridional overturning circulation in the model. Figures S3 to S5 show the spatial and depth-dependent distribution of $\delta^{18}O$ in the 100% N Atlantic, 30:70 Atlantic:Antarctic, and 100% Antarctic melt-water release scenarios for standard model-parameter values (50:50 is elaborated in main text), as discussed in the main text. Figure S-6 illustrates the mean $\delta^{18}O$ developments in all ocean basins for the various scenarios. Fig. S-7 is like main-text figure 3, but then for the sensitivity tests with $\delta^{18}O$ values for Antarctic and Greenland melt water of –50‰ and –30‰, respectively.

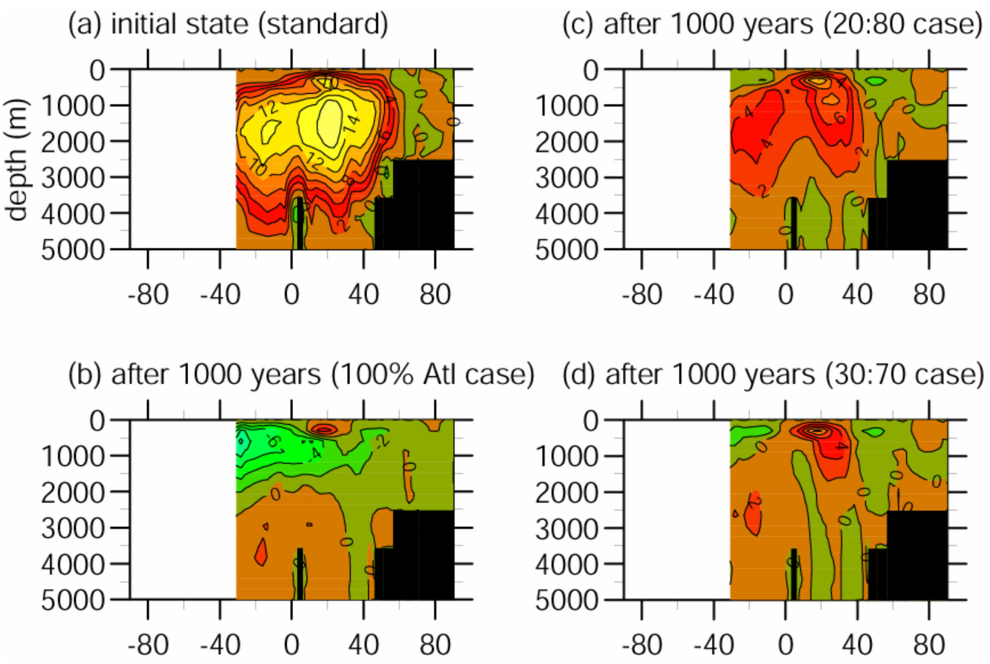

Figure S-1. Atlantic meridional overturning streamfunctions under "standard" parameters. **(a)** Initial state, where deep sinking in the zone 40-60°N contributes 12 Sv to the total overturning, which is dominated by an interhemispheric cell. **(b)** Extreme scenario with 100% melt-water release into the N Atlantic. The overturning circulation collapses entirely and intermediate water from the Southern Ocean invades the Atlantic up to 50°N. **(c)** Scenario with 20% melt-water release to the N Atlantic. Overturning is partially collapsed, with weaker sinking confined south of 40°N. **(d)** Scenario with 30% release into the N Atlantic, giving similar conditions to(c), albeit more pronounced.

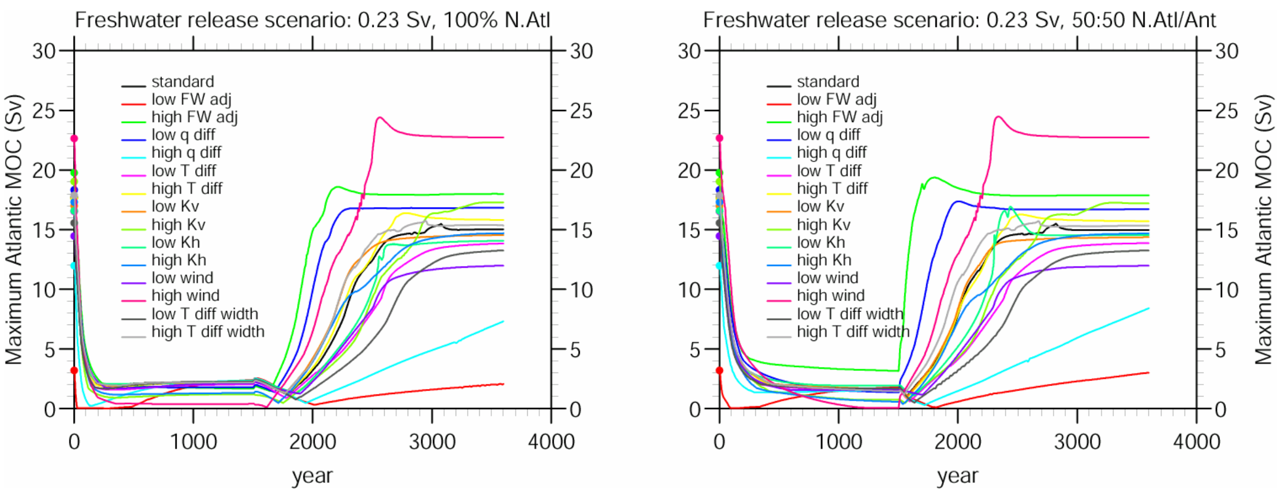

Figure S-2. Time series of maximum Atlantic overturning in the 100% N. Atlantic (left panel) and 50:50 Atlantic:Antarctic (right panel) melt-water release scenarios, in the standard case and for 14 alternative high/low values of each key parameter. In all 30 cases the Atlantic overturning collapses rapidly, showing that collapse is robust across a wide range of values for seven key model parameters.

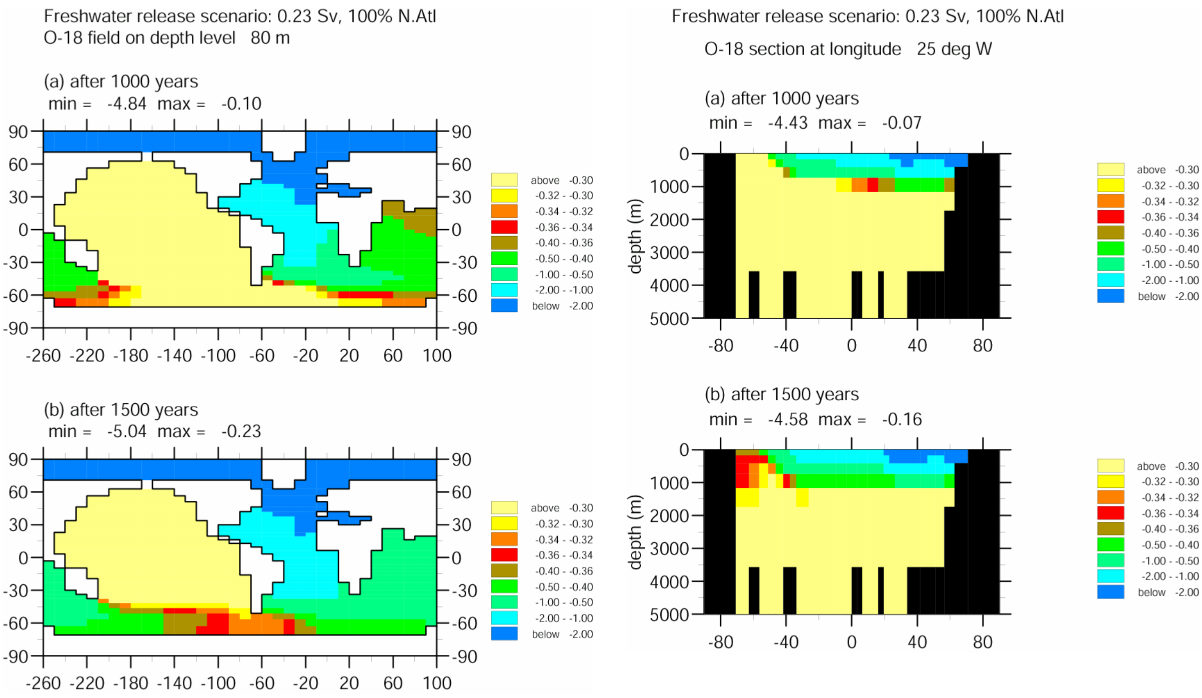

Figure S-3. Maps and sections of $\delta^{18}O$ distribution after 1000 and 1500 years in the scenario with 100% melt-water release into the N Atlantic (0.23 Sv for 1500 years). Negative $\delta^{18}O$ values remain confined to the upper layers of the North Atlantic, inefficiently removed from the source region through slow mixing processes and weak southward surface flow (see Figure S-1b)

Figure S-4. As Figure S-3, for the scenario with 30% melt-water release into the N Atlantic, and 70% around Antarctica. The north shows reduced overturn, which still penetrates deeper than 2000 m, and in the south the Antarctic signal is efficiently transported downwards as convection and deep sinking are little affected by the freshwater forcing.

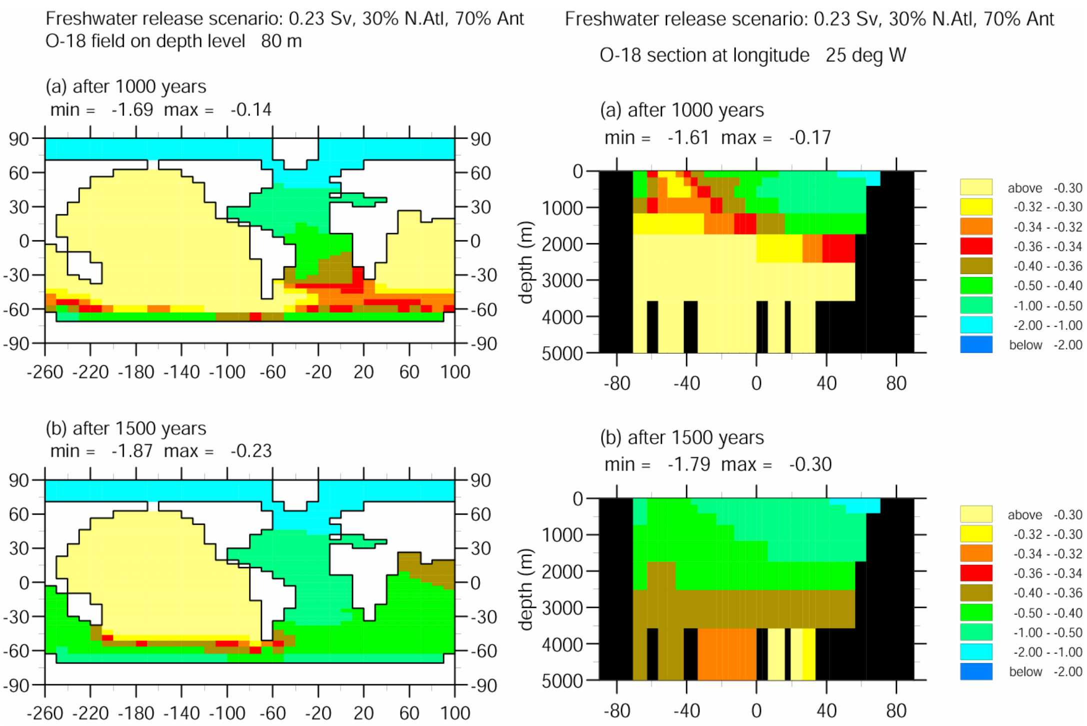

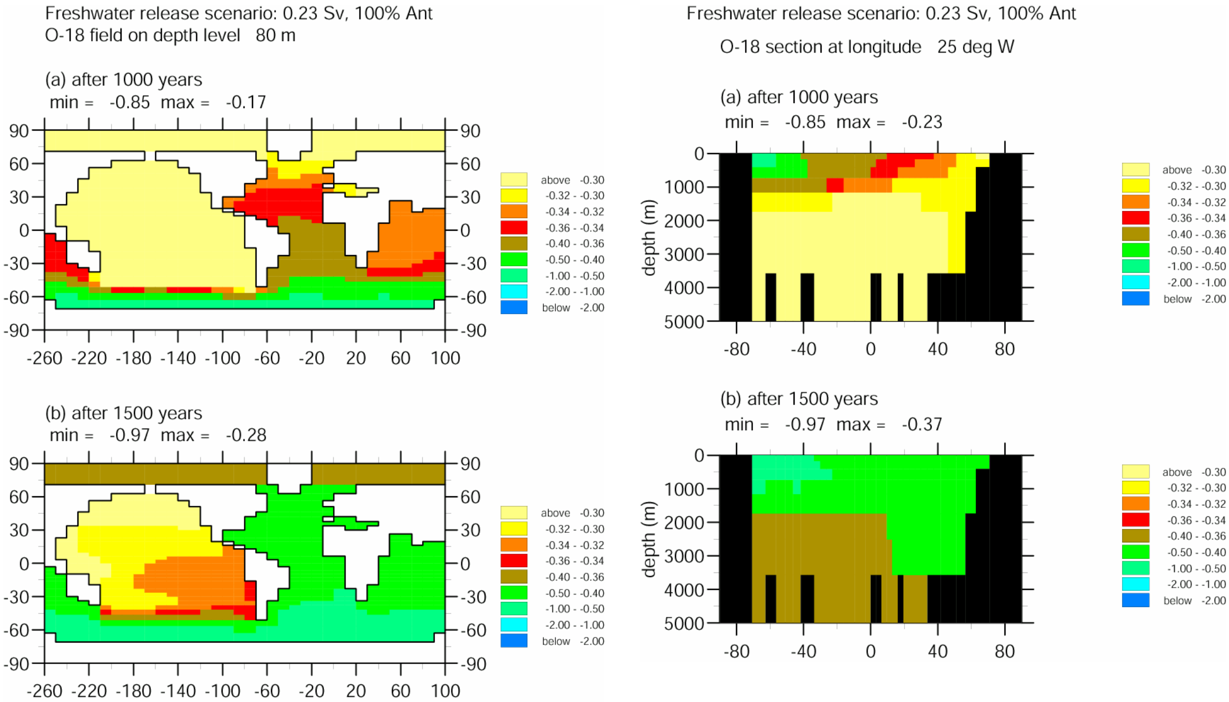

Figure S-5. As Figures S-3 and S-4, for the scenario with 100% melt-water release around Antarctica. There are no great δ^{18}O anomalies due to efficient mixing throughout the Southern Ocean.

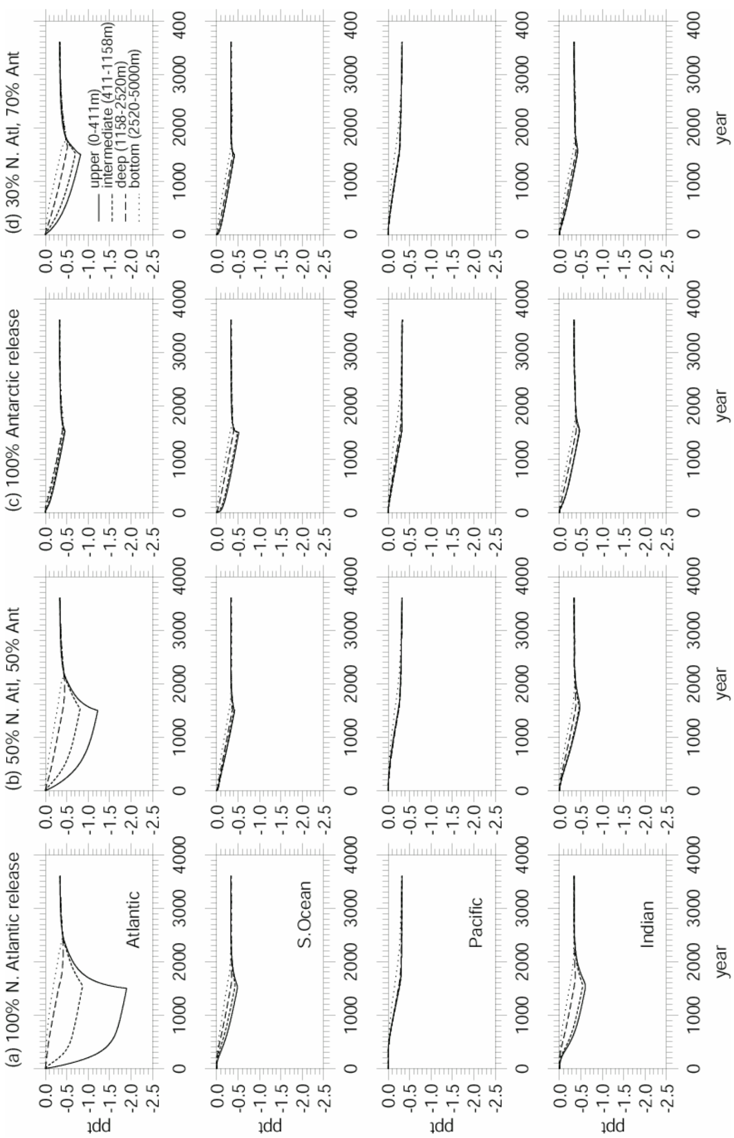

Figure S-6. As figure 2 in the main text, but with profiles for the mean δ^{18}O developments versus time in all ocean basins.

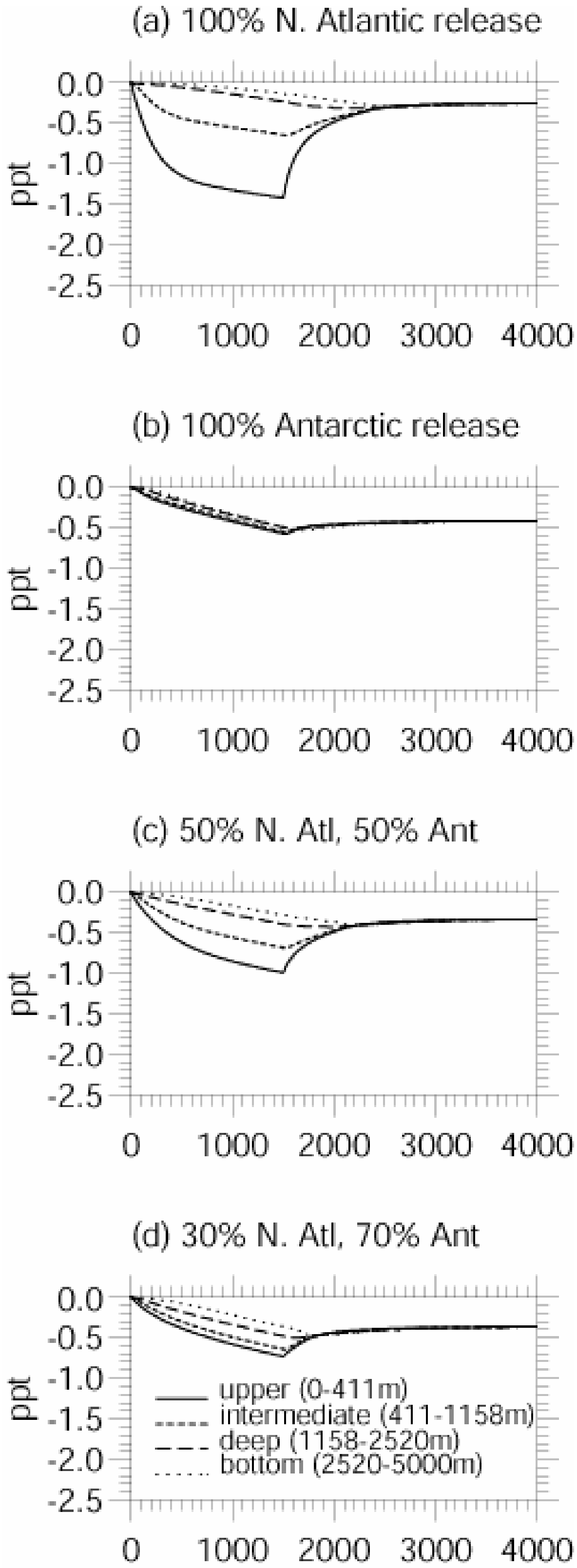

Figure S-7. As figure 2 in the main text (but including the 30:70 scenario), to illustrate the impact of changing $\delta^{18}O$ values of Antarctic and Greenland melt-water to –50‰ and –30‰, respectively.

References to the Supplementary Information

All references are numbered as they appeared in the main article text. Additional references used here are numbered to sequentially follow those of the main text.

31. Hagen, S. & Hald, M. Variation in surface and deep water circulation in the Denmark Strait, North Atlantic, during marine isotope stages 3 and 2, *Paleoceanography* **17**, DOI 10.1029/2001PA000632 (2002).
32. Vidal, L., Labeyrie, L. & Van Weering, T.C.E. Benthic δ^{18}O records in the North Atlantic over the last glacial period (60-10 kyr): evidence for brine formation, *Paleoceanography* **13**, 245-251 (1998).
33. Rasmussen, T.L., Oppo, D.W., Thomsen, E. & Lehman, S.J. Deep sea records from the southeast Labrador Sea: ocean circulation changes and ice-rafting events during the last 160,000 years, *Paleoceanography* **18**, DOI10.1029/2001PA000736 (2003).
34. Hüls, M. & Zahn, R. Millennial-scale sea surface temperature variability in the western tropical North Atlantic from planktonic foraminiferal census counts, *Paleoceanography* **15**, 659-678 (2000).
35. Vidal, L., Schneider, R.R., Marchal, O., Bickert, T., Stocker, T.F. & Wefer, G. Link between the North and South Atlantic during the Heinrich events of the last glacial period, *Clim. Dyn.* **15**, 909-919 (1999).
36. Little, M.G., Schneider, R.R., Kroon, D., Price, B., Summerhayes, C.P. & Segl, M. Trade wind forcing of upwelling, seasonality, and Heinrich events as a response to sub-Milankovitch climate variability, *Paleoceanography* **12**, 568-576 (1997).
37. Voelker, A.H.L., Grootes, P.M., Nadeau, M.J. & Sarnthein, M. Radiocarbon levels in the Iceland Sea from 25-53 kyr and their link to the earth's magnetic field intensity, *Radiocarbon* **42**, 437-452 (2000).
38. Elliot, M. Laberie, L., Bond, G., Cortijo, E., Turon, J.L., Tisnerat, N. & Duplessy, J.C. Millennial-scale iceberg discharges in the Irminger Basin during the last glacial period: Relationship with the Heinrich events and environmental settings, *Paleoceanography* **13**, 433-446 (1998).
39. Dokken, T.M. & Jansen, E. Rapid changes in the mechanism of ocean convection during the last glacial period, *Nature* **401**, 458-461 (1999).
40. Grousset, F.E., Cortijo, E., Huon, S., Hervé, L., Richter, T., Burdloff, D., Duprat, J. & Weber, O. Zooming in on Heinrich layers, *Paleoceanography* **16**, 240-259 (2001).
41. Charles, C.D., Lynch-Stieglitz, J., Ninnemann, U.S. & Fairbanks, R.G., Climate connections between the hemispheres revealed by deep sea sediment core/ ice core correlations, *Earth Planet. Sci. Lett.* **142**, 19-27 (1996).
42. Edwards N.R. & Shepherd, J.G. Bifurcations of the thermohaline circulation in a simplified three-dimensional model of the world ocean and the effects of interbasin connectivity. *Clim. Dyn.* **19**, 31-42 (2002).
43. Weaver A.J., Eby M., Wiebe E.C., Bitz C.M., Duffy P.B., Ewen T.L., Fanning A.F., Holland M.M., MacFadyen A., Matthews H.D., Meissner K.J., Saenko O., Schmittner A., Wang H. & Yoshimori M. The UVic Earth System Climate Model: Model description, climatology, and applications to past, present and future climates. *Atmos. Ocean* **39**, 361-428 (2001).
44. Semtner A.J. A model for the thermodynamic growth of sea ice in numerical investigations of climate. *J. Phys. Oceanogr.* **6**, 379-389 (1976).
45. Hibler W.D. A dynamic thermodynamic sea ice model. *J. Phys. Oceanogr.* **9**, 815-846 (1979).
46. Hargreaves, J.C., Annan, J.D., Edwards, N.R., and Marsh. R. Climate forecasting using an intermediate complexity Earth System Model and the ensemble Kalman filter. *Clim. Dyn.*, submitted. (2004).